Materials Chemistry and Physics 340 (2025) 130844

Contents lists available at ScienceDirect

Materials Chemistry and Physics

journal homepage: www.elsevier.com/locate/matchemphys

Experimental and numerical study of dissimilar laser welding characterisation of ASTM B637 and duplex 2205

Amir Parsian [a], Mohammad Akbari [a,b,*], Arash Karimipour [a,b], Mahdi Rafiei [c], Mohammad Mehdi Razzaghi [a,b]

[a] Department of Mechanical Engineering, Najafabad Branch, Islamic Azad University, Najafabad, Iran
[b] Aerospace and Energy Conversion Research Center, Najafabad Branch, Islamic Azad University, Najafabad, Iran
[c] Advanced Materials Research Center, Department of Materials Engineering, Najafabad Branch, Islamic Azad University, Najafabad, Iran

HIGHLIGHTS

- Laser welding of ASTM B637 and duplex 2205 in a circular geometry was studied.
- Temperature distribution, molten pool geometry and the microstructural changes were investigated.
- Experimental measurements validated the numerical simulations.
- Microstructural analysis revealed a transition from columnar dendrites to a cellular structure.
- Tensile strength and elongation properties exhibited notable improvements with increased laser power.

ARTICLE INFO

Keywords:
ASTM B637
Dissimilar laser welding
Duplex 2205
Microstructure analysis
Response surface methodology (RSM)

ABSTRACT

This study presents a comprehensive investigation into the impact of dissimilar fibre laser welding parameters on the thermal and mechanical characteristics of ASTM B637 nickel-based alloy and duplex 2205 stainless steel in a circular geometry. A central composite design (CCD) approach was employed to systematically examine the effects of the key process parameters on the responses of melt pool geometry, temperature field near the melt pool, and joint tensile stress and strain. Numerical simulations were conducted to evaluate temperature distribution inside the fusion zone, molten pool geometry and the microstructural changes according to the temperature gradient induced by heating and solidification process. The results demonstrated that increasing laser power from 300 to 400 W led to a significant increase in the depth of the melt pool from 1 to 1.5 mm. Experimental measurements validated the numerical simulations, confirming their accuracy in predicting temperature gradients and molten pool behaviour. The temperature near the melt pool of both metals had experienced more than 200 °C temperature variation by increasing the laser power from 200 to 400 W. At high welding speed of 500 mm/min, a lower temperature level about 50 °C was observed for the duplex side because of having more heat sink effect. Microstructural analysis revealed a transition from columnar dendrites near the fusion boundary to a cellular structure toward the fusion zone centre, driven by variations in solidification intensity. Furthermore, tensile strength and elongation properties exhibited notable improvements with increased laser power. A rise of laser power from 250 to 450 W resulted in a tensile strength increase from 330 MPa to 570 MPa, while elongation improved from 3 % to 19 %. These findings emphasize the critical role of laser power and welding speed to improve weld quality and mechanical performance.

1. Introduction

Duplex stainless steel (DSS) 2205 has attracted a lot of attention because it combines strong mechanical properties, good corrosion resistance, and cost-effectiveness, making it stand out compared to traditional stainless-steel grades (e.g. austenitic or ferritic). With its higher tensile strength, and greater yield strength, it's often the preferred choice in industries like oil and gas, marine applications, and

---

* Corresponding author. Department of Mechanical Engineering, Najafabad Branch, Islamic Azad University, Najafabad, Iran.
E-mail address: m.akbari.g80@gmail.com (M. Akbari).

https://doi.org/10.1016/j.matchemphys.2025.130844
Received 20 December 2024; Received in revised form 23 March 2025; Accepted 2 April 2025

construction [1–6]. The ASTM B637 alloy, on the other hand, is a nickel-based superalloy that's a staple in the aerospace industry because it can handle creep, oxidation, and thermal fatigue even at high temperatures. Thanks to these qualities, it often outperforms traditional nickel-based superalloys in tough applications [7]. Thus, dissimilar welding between DSS 2205 and ASTM B637 presents opportunities to create joints that withstand extreme service conditions.

Fibre laser welding has become an essential technique for joining, achieving reliable welds between DSS and nickel-based superalloys isn't straightforward, it requires careful control over key factors like laser power, welding speed, focal length, beam deflection, pulse duration, and the choice of shielding gas [8–11]. While previous research has looked closely at these parameters, there is still a limited understanding of how they specifically affect dissimilar welds between DSS 2205 and ASTM B637. Saravanan et al. [5] examined the synergistic effects of the incident beam power irradiated the workpiece surface and velocity of welding on super duplex stainless steel utilizing a YAG laser at pulsed mode. Their findings indicated that increased heat input facilitated full penetration, resulting in enhanced weld quality. Odermatt et al. [12] investigated the microstructure and mechanical properties of laser beam welded butt joints in 4 mm thick duplex stainless steel 2205. Their study revealed a fully ferritic fusion zone and increased microhardness in the weld area. Although welded specimens showed higher strength but lower ductility than the base metal, fatigue performance was reduced due to weld geometry. However, laser surface remelting improved fatigue resistance to levels comparable with the base material. Baghdadchi et al. [13] explored how laser reheating affected FDX 27 duplex stainless-steel welds and found that using nitrogen as a shielding gas boosted austenite formation while reducing the formation of brittle nitride phases. Calliari et al. [14] and Ghorsh et al. [15] focused on welding Duplex 2205 b y implementing YAG laser, concluding that an increase in pulse width resulted in a reduction in weld strength and bead width. Gozarganji et al. [16] demonstrated that using a nitrogen shielding gas blend during pulsed laser welding of 2205 DSS helped improve microstructural properties and increased hardness at the weld centreline. Ahmad et al. [17] investigated laser beam welding of the joints between duplex steel sheet and Inconel 625, reinforcing the idea that carefully controlling laser parameters is crucial for achieving strong, defect-free dissimilar welds.

Vemanaboina et al. used a CO_2 laser welding process and discovered that managing the heat input effectively reduced distortion and minimized defects in the weld. Azari et al. [18] focused on how laser power influenced temperature distribution and microstructural changes in laser-welded Inconel 625, highlighting its role in refining the microstructure and improving mechanical properties. Thejasree et al. studied the impact of laser parameters on tensile stress of Inconel 718 weld joint and its dimensional geometry, offering valuable insights into optimizing these parameters. Corigliano et al. examined the fatigue characterization of laser-welded joints between Ti6Al4V and Inconel 625, using a thermographic approach to predict fatigue strength. Their results confirmed that these dissimilar welds have high resistance to fatigue, highlighting the importance of optimizing welding parameters to achieve strong, reliable joints. Building on these findings, this study offers a comprehensive look at the temperature distribution and weld characteristics of DSS 2205 and ASTM B637 joints using fibre laser welding. Sharma et al. [19] investigated the fusion zone microstructural changes of Inconel 718 at different laser welding speeds. They observed columnar dendrite at the welded joint interface with base metal and dendritic microstructure with equiaxed morphology at the fusion zone center. At the interdendritic regions, the inter-columnar and gamma prime precipitates existed. Madhankumar et al. [20] investigated the ultimate tensile strength of laser beam welded Inconel 718 and duplex 2205 stainless steel joints, which are widely used in petroleum, energy storage, and coastal applications. The influence of laser power, welding speed and focal position on tensile strength was investigated via experimental. The results showed that optimized welding parameters significantly enhanced tensile properties, with analysis of variance (ANOVA) used to determine the optimal joint strength.

Shen et al. [21] examined the microstructure and mechanical properties of 2205 DSS/Inconel 718 dissimilar laser-welded joints for subsea applications. SEM analysis revealed the formation of irregular Laves phases, with a well-fused Inconel 718-weld interface and a distinct transition zone at the 2205 DSS-weld interface. Corrosion tests results showed a 41 % reduction in corrosion current density, improving corrosion resistance. Hardness increased by 19.1 %, but elongation decreased due to Laves phase brittleness. Ghosh et al. [22] conducted an experimental study on pulsed Nd:YAG laser welding of 2205 duplex stainless steel, analysing the effects of welding speed on weld quality while keeping laser power and pulse width constant. Their findings showed that weld strength increases with scanning speed up to a certain point before declining. Additionally, penetration depth and bead width decreased with increasing scanning speed. Microstructural analysis revealed a higher ferrite content and lower austenite content due to rapid cooling. Vickers hardness tests indicated a gradual decrease in hardness from the fusion zone to the base material, correlating with metallurgical phase changes.

The main objective of this research is evaluation of the weld characterization at circular geometry for creating dissimilar joint between duplex stainless steel (DSS) 2205 and ASTM B637 through experimental and numerical analysis. To examine the effect of process parameters on the quantitative response of temperature near the melt pool, joint tensile stress and strain rate, weld bead and melt pool geometry, and microstructure of the fusion zone, the central composite design (CCD) approach was implemented to systematically assess the influence of critical welding parameters. The numerical simulations approach was implemented to analyse the temperature gradients within the melt pool, allowing the prediction of melt pool geometry according to the melting of materials through phase transformation created via temperature gradient, and thereby the resultant microstructure created via heating and cooling cycles which determine the solidification rate. Due to the existing asymmetrical temperature field induced by different material volume and geometry, the numerical simulation of temperature distribution could be more influential compared to simple and symmetrical weld metals geometry.

Although numerical simulation of temperature gradient in the dissimilar laser welding of nickel base alloys and duplex stainless steel has been performed in previous studies [23–26], there is no study which investigated the dissimilar ASTM B637 and duplex 2205 at circular geometry. Furthermore, the relation between the temperature distribution and melt volume participation of each dissimilar material has not been performed in previous studies in cases where the material volume and heat sink capacity have had evident discrepancy. This highlights the importance of the present study's focus on asymmetrical heat distribution and its impact on weld characteristics, particularly under conditions of differing material volumes and thermal properties. Despite prior research on dissimilar welding, a detailed assessment of the mechanical and microstructural characteristics of these welded joints remains limited. To bridge this gap, the present study provides an in-depth analysis of the impact of key laser parameters on heat distribution, weld morphology, and overall joint integrity, particularly in circular weld geometries where material volume differences influence heat dissipation. By integrating experimental validation with numerical modeling, this research aims to optimize welding conditions, thereby enhancing weld quality and structural reliability in DSS 2205 and ASTM B637 joints.

2. Experimental procedure

For the welding of dissimilar materials, a single-mode fiber laser model YLPS made by GW-laser with the power output of 750 W was employed. The laser beam transmitted to the (BW210 -RAYTOOLS) head for laser welding through a QBH connector. A side nozzle was

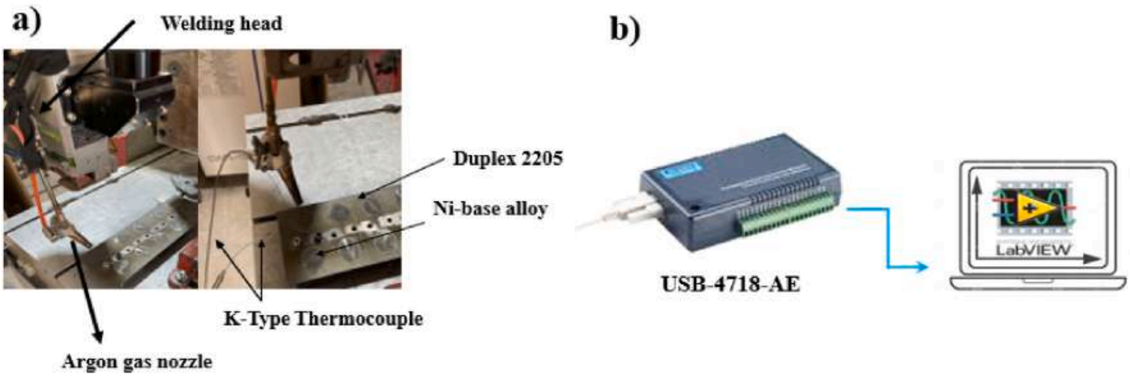

Fig. 1. Laser instruments of welding process, a) actual view, b) schematic.

Table 1
Chemical composition of the alloys.

Element (% W)														
Alloy	CO	Si	Mn	P	Al	Cr	Fe	Mo	C	Ti	Zr	s	B	Ni
Ni-base Alloys	14	0.05	0.5	–	1.45	20.5	1.1	4.7	0.1	2.9	0.1	0.02	0.003	Balance
	Si	Mn	P	Al	Cr	Ni	Mo	s	C					
Duplex 2205 steel	1	2.00	0.03	0.03	23	6.5	3.5	0.02	0.03					

Table 2
Selected parameters level for CCD.

No	Power (W)	Velocity (mm/min)	Focal Distance (mm)	Deviation (mm)
1	250–450	200–500	−1.5- +4.5	−0.5-+0.5

implemented to protect the melted fusion zone by protection via argon gas flow. To accurately position both workpieces, a specialized fixture was utilized to secure the dissimilar metals and thermocouples, as illustrated in Fig. 1. The nickel-based circular sheets with a diameter of 20 mm are centrally located within a duplex steel matrix. The thermocouples from K-type grade and 1 mm tip diameter made by Taizhou are situated 2 mm away from the middle of the fusion region. The thermocouples wires were connected to the Advantech USB 4718 card (made by National Instruments), which ultimately recorded the analogue signal using LABVIEW software.

Table 1 represents both duplex 2205 stainless steel and nickel-base alloy chemical composition based on weight percentage. The metal analyser model (SPECTRO LAB-S) was used to extract the materials chemical composition.

For the metallographic examination of the weld cross-section, an Olympus inverted microscope was utilized. The preparation of the welded samples adhered to the ASTM E3-11 standard. The weld bead surface images were obtained via SZX18 Olympus stereoscope. Microstructure of the joint melt pool and adjacent regions, along with EDS analysis, was conducted using MIRA-FESEM-3rd generation made by TESCAN. Tensile testing of the welded samples was carried out with a universal tensile testing machine (GOTECH AI-7000), following the ASTM E8 standard. The experimental design method was central composite design, comprising 28 experiments and their respective levels, as detailed in Table 2. The responses of maximum temperature measured on each base metal via thermocouples, the tensile strength of produced dissimilar joints and the maximum melt pool penetration were analysed.

3. Numerical modelling

This study employed computational fluid dynamics (CFD) to simulate the laser welding technique utilizing the finite volume method. The numerical computation was executed using the commercial computational fluid dynamics software Ansys Fluent. User-defined functions (UDF) implemented in the C programming language were utilized to derive the source terms in the governing equations, boundary conditions, and variable thermophysical properties. The model considered various processes related to welding, including temperature-dependent material properties and heat losses from convection and radiation. The enthalpy-porosity technique was used to simulate the melting and solidification process during laser welding. The SIMPLE algorithm was employed to couple the velocity and pressure fields. The convergence accuracy for all equations was deemed to be 10^{-4}. The time increment was 10^{-4} s, and the number of iterations per time increment was dictated by the convergence criteria.

3.1. Modelling of the laser beam

The laser beam has been considered as a means of cylindrical heat source according to equation (1).

$$q_v(x,y,z) = \frac{6f_2\eta p}{\pi r_v^2 d}\, exp\left(-3\frac{(x^2+y^2)}{r_v^2}\right)\left(\frac{mz+r_v}{md+2r_v}\right) \tag{1}$$

The term $q_v(x,y,z)$ represents the volumetric heat source term $[W/m^3]$. f_2 is the heat source intensity factor, and η denotes the laser absorption efficiency, p is the laser power $[W]$, while r_v refers to the effective laser beam radius $[mm]$. d is the characteristic penetration depth $[mm]$. The coordinates x,y,z define the spatial position in the Cartesian system, with z representing the depth direction. The term m is a geometric correction coefficient accounting for beam divergence.

The below equations are derived from the following assumptions. The molten pool surface is presumed to remain flat. Additionally, the thermo-physical properties are assumed to vary as a function of temperature. The primary default temperature is taken to be 298 K.

Continuity equation:

$$\nabla.\left(\rho\vec{U}\right) = 0 \tag{2}$$

where ρ represents the fluid density $[kg/m^3]$, and U is the velocity vector with components (u,v,w) in the x, y, and z directions, respectively. The operator ∇ denotes the divergence of the velocity field, ensuring mass conservation in the fluid domain.

Momentum equation:

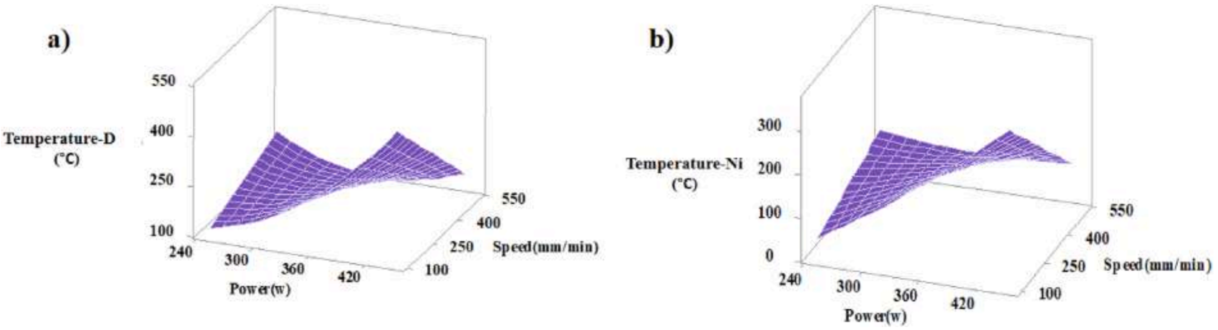

Fig. 2. The welding speed and beam power impact on the temperature of a) duplex steel, b) ASTM B637 alloy.

$$\frac{\partial\left(\rho\vec{U}\right)}{\partial t}+\nabla.\left(\rho\vec{U}\vec{U}\right)=-\nabla \text{p}+\nabla.\left(\mu\nabla\vec{U}\right)+\rho\vec{g}-\frac{\mu}{K}\left(\vec{U}\right) \tag{3}$$

Where $\rho, t, \vec{U}, p, \vec{g}, \mu, K$ include density $[{kg}/{m^3}]$, time, velocity vector $[m/s]$, pressure $[Pa]$, gravitational acceleration vector $[m/{s^2}]$, dynamic viscosity $[Pa.s]$, and the Darcy resistance coefficient, orderly.

Energy equation:

$$\frac{\partial(\rho H)}{\partial t}+\nabla.\left(\rho\vec{U}H\right)=\nabla.(k\nabla T) \tag{4}$$

In Equation (4), H is the total enthalpy *[J]*, T is the temperature *[K]*, and k is the thermal conductivity $[{W}/{m\,K}]$.

3.2. Boundary conditions

The boundary condition at the sheet's surface is established via thermal model under consideration (Eq. (5)).

$$k\frac{\partial T}{\partial \vec{n}}=-\varepsilon\sigma\left(T^4-T_\infty^4\right)-h(T-T_\infty) \tag{5}$$

In Equation (5), ε represents the emission coefficient, σ denotes the Stefan-Boltzmann coefficient $[{W}/{m^2\,K^4}]$, T_∞ indicates the environmental temperature and h signifies the heat transfer coefficient $[{W}/{m^2\,K}]$.

$$\mu\frac{\partial u}{\partial z}=-\frac{\partial\gamma}{\partial T}\frac{\partial T}{\partial x} \tag{6}$$

$$\mu\frac{\partial v}{\partial z}=-\frac{\partial\gamma}{\partial T}\frac{\partial T}{\partial y} \tag{7}$$

In Equations (6) and (7), u and v represent velocity of the x, y directions and $\frac{\partial\gamma}{\partial T}$ implies on the tension gradient of the surface *[Pa/K]*.

4. Result and discussion

This research examines the influence of laser beam welding parameters on the characterization of weld quality through both experimental and numerical methods. The study focuses on the dissimilar laser welding process, investigating the temperature in proximity to the fusion line, the microstructure of the dissimilar joint fusion area, as well as the weld joint mechanical properties through experimental analysis. Furthermore, numerical simulations were employed to evaluate the fusion zone and the surrounding areas temperature map. The dissimilar joint produced between duplex 2205 stainless steel and nickel-based alloy by laser welding, characterized by a circular and asymmetric geometry, presents significant challenges due to the differing properties of the materials involved. Notably, duplex stainless steel has a melting point that is approximately 100 °C higher than that of the nickel-based alloy, and the two materials exhibit different levels of laser energy absorption. These variations contribute to the complexity of welding such joints. Consequently, the application of numerical simulations to assess the temperature distribution in the melt pool and its surroundings is essential for predicting weld geometry and comprehending the resultant microstructure.

4.1. The laser parameters impact the ambient temperature of the fusion region

The influence of laser power and linear velocity on the peak temperature recorded by thermocouples located at 2 mm distance from the middle of the fusion zone illustrated in Fig. 2a. An evident rise of the beam power level from lower levels up to 350 W did not result in notable variations in the duplex steel temperature. However, elevation of the power up to 400 W, created a significant rise of the temperature from

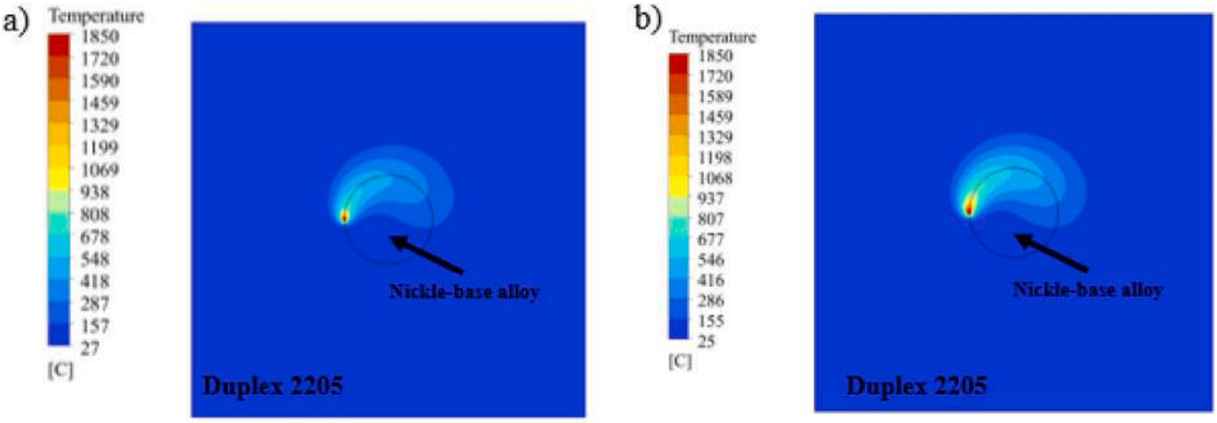

Fig. 3. The temperature field distribution at the top surface for the laser power of a)300 W, b) 400 W.

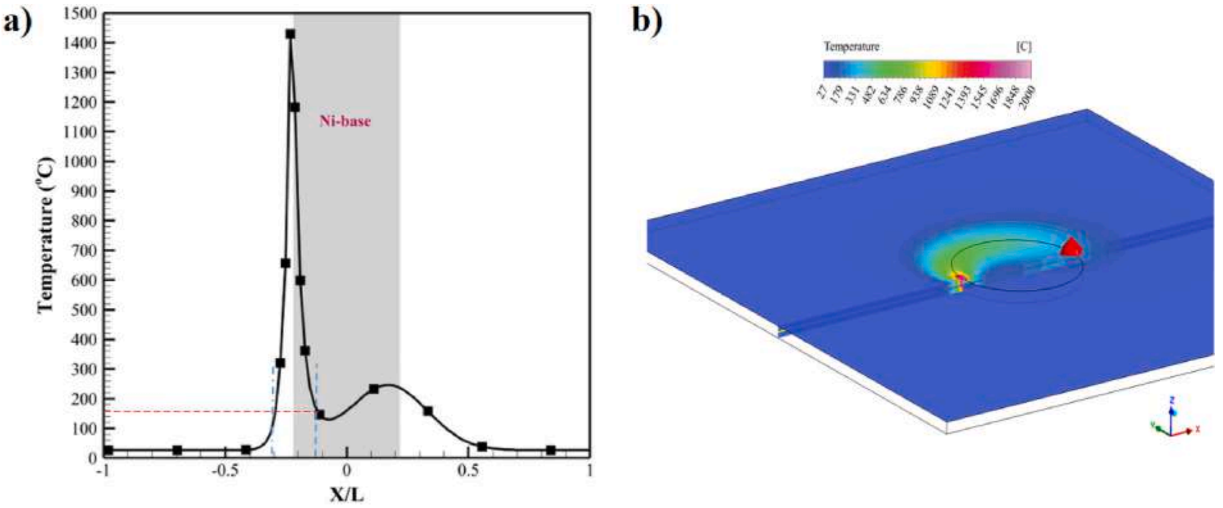

Fig. 4. The dissimilar joint temperature history across a) the workpiece thickness and b) temperature distribution.

150 °C to 380 °C. At this power setting, the duplex steel experienced adequate melting, achieving its peak temperature. Additionally, laser increasing the laser velocity at this power level, reduced the duplex steel thermocouples temperature from 380 °C to 200 °C. Therefore, both beam power and weld linear velocity are critical factors that can lead to significant temperature variations around the molten pool. It is noteworthy that changes in welding speed had a more pronounced impact compared to changes in laser power at the 400 W setting.

Fig. 2b illustrates the laser power and beam velocity effect on the measured temperature of the thermocouples on the ASTM B637 alloy. It was observed that an increase of about 150 W in laser power level from 250 W, led to a temperature increase of approximately 200 °C around the molten pool. However, at a speed of 200 mm/min, the temperature rises significantly decreased as the welding speed was further raised, resulting in a temperature rise of only 40 °C at a speed of 400 mm/min. In contrast, at a laser power of 250 W, variations in welding speed had a negligible effect on the temperature fluctuations of the ASTM B637 alloy.

This is because of inadequate materials melting at low laser power, where speed changes had a limited effect on temperature fluctuations around the molten pool. This behaviour could be ascribed to the insufficient melting of the two materials at low laser power levels, which resulted in the reduced sensitivity of temperature changes to variations in the welding speed.

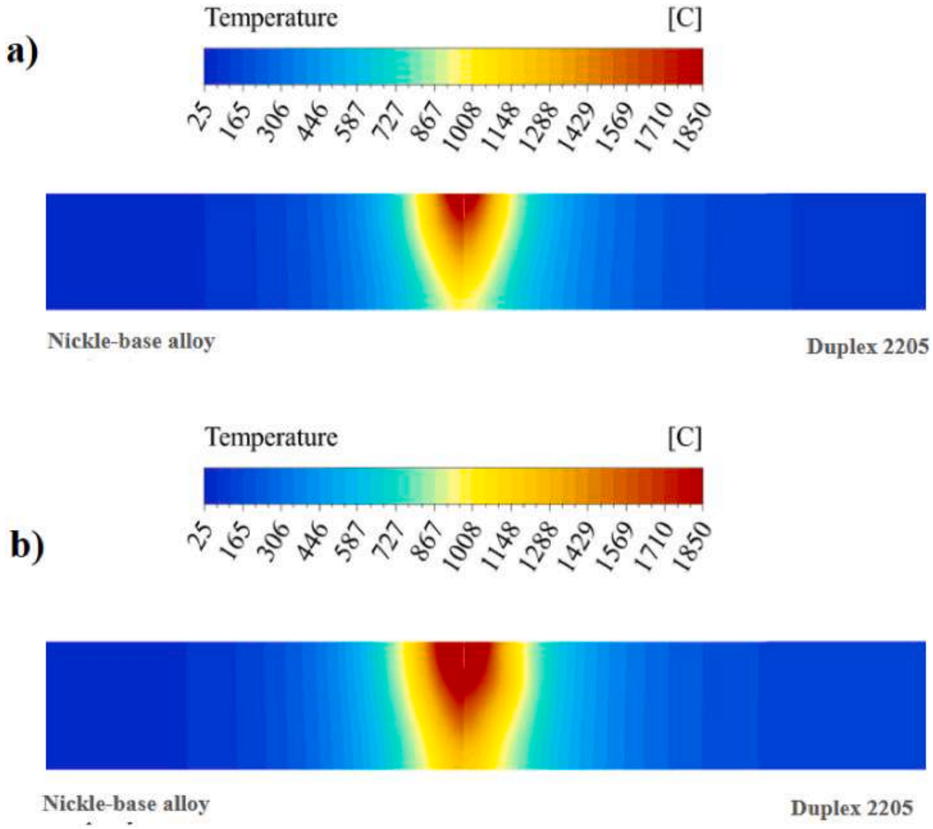

Fig. 5. The weld cross-section temperature distribution for different laser powers of a) 300 W, b) 400 W.

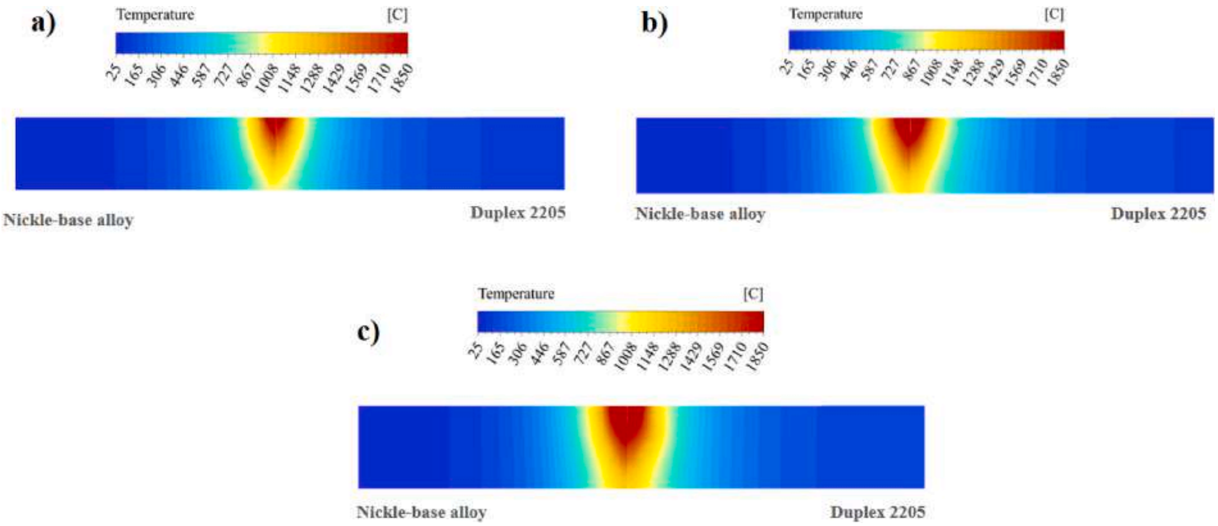

Fig. 6. The effect of increasing laser power on the temperature field at the cross section of the weld at laser power of a)300 W, b)350 W, c) 400 W.

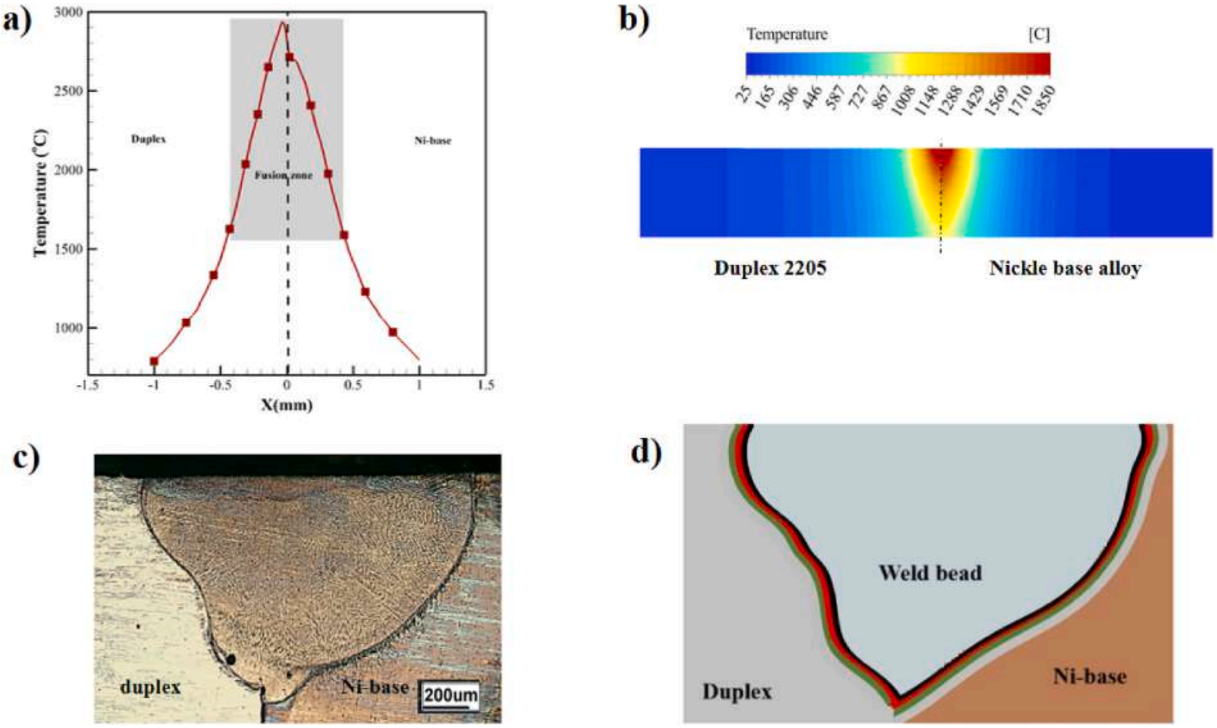

Fig. 7. Comparison of the temperature field and melt pool geometry at a laser power of 350 W, a) temperature distribution graph from 1 mm distance to the fusion zone, b) temperature field from both base metals to the fusion zone, c) the experimental melt pool appearance, d) predicted melt pool shape.

Fig. 3 presents a distinct comparison of the temperature distribution on the upper surface of the workpiece as the laser power is raised from 300 W to 400 W. It is observed that the higher temperature region above 670 °C (see Fig. 3b), has been extended to wider and longer regions where the thermocouples measure the temperature on both alloys. Additionally, at a higher laser power of 400 W, total heat accumulation is greater, especially on the Ni-base alloy side, due to lower heat conduction and a smaller surface area.

Fig. 4 illustrates the temperature history of dissimilar welded regions at half of the material thickness. The nickel base boundaries were highlighted in Fig. 4b and the temperature history at different locations of the line through half of the workpiece thickness is observed. A distance of 2 mm from the boundaries of the nickel base alloy is pointed out in Fig. 4a. It is clearly observed that the temperature at this distance at both base metals has had a slight discrepancy, although the temperature for both parts was lower than 200 °C. Furthermore, it could be said that the temperature gradient and its fluctuation at the Ni-base alloy side have been incredibly more than the duplex workpiece as shown in Fig. 4a. On the other hand, it could be said that the high-temperature region at the heat-affected zone of duplex steel is relatively higher for duplex steel compared with Ni-base alloy as shown in Fig. 4a.

The cross-section of the temperature field for both metals is illustrated in Fig. 5. It can be observed that the higher region temperature of duplex steel has been extended more at the duplex steel side by about 30 percent for the duplex side compared to the Ni-base alloy when the laser power increased from 300 to 400 W. Therefore, it can be concluded that at the same condition, the temperature of the duplex is relatively higher due to having different thermophysical properties. The higher thermal

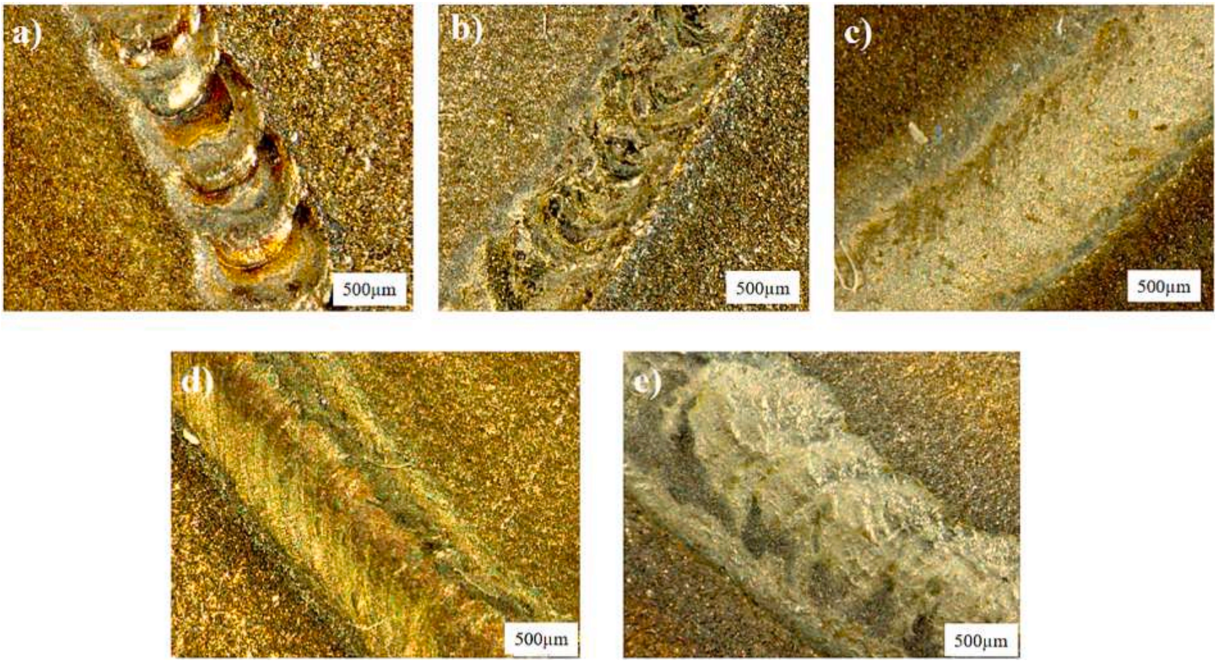

Fig. 8. The weld bead appearance at the speed of 300 mm/min and focal distance at different laser powers of a) 300 W, b)350 W, c)400 W, and at laser powers of 400 W at various speed of d) 300 mm/min, e) 200 mm/min.

conductivity of duplex 2205 and its higher melting point results in the dissipation of higher temperature toward the base metal of duplex steel and thereby the temperature at the target points reached higher values as shown in both experiments and numerical results.

Fig. 6 illustrates the impact of power enhancement on the temperature distribution at the cross-section of the weld joint, which encompasses both dissimilar metals in terms of width and depth concurrently. It is clearly evident that the area exhibiting temperatures exceeding 1400 °C significantly expanded at a laser power of 400 W in comparison to 300 W. Additionally, Fig. 6 demonstrates the relationship between the increasing depth and width of the melt pool as the laser power rises from 250 to 400 W, as observed in the comparison between Fig. 6a and c.

4.2. *Formation of the melt pool according to the temperature field*

Fig. 7 demonstrates a distinct relationship between experimental findings and numerical results regarding the temperature distribution and fusion zone formation at laser power of 350 W. In Fig. 7a, the anticipated temperature distribution is illustrated for the region that spans from the heat-affected zone (HAZ) to the midpoint of the fusion zone. The data presented in Fig. 7a reveals that the temperature recorded at a distance of 1 mm from the center of the melt pool on either side of the base metals did not exceed 800 °C. This indicates that melting did not take place at this distance, and only the heat-affected zones are discernible.

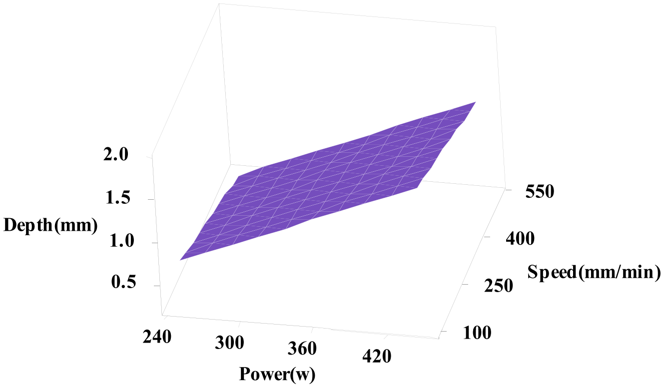

Fig. 9. The laser power and beam speed on the melt pool depth.

At a distance of 2 mm, where the thermocouples are located, the temperature is comparatively lower. The fusion line temperature for both base metals exceeds 1500 °C and increases to levels where the melted materials may evaporate.

The elevated energy of the laser beam results in greater absorption by the molten material, potentially raising the temperature to levels exceeding 2000 °C. Conversely, Fig. 7c illustrates that the width of the melt pool at the upper surface is approximately 1 mm, which aligns with the temperature surpassing the melting point of both metals, exceeding 1500 °C.

A comparison of Fig. 7a–b demonstrate that the high-temperature area at Ni-base alloy is bigger than the duplex side while the maximum temperature of the Ni-base side is relatively lower than the duplex.

Comparison of Fig. 7c–d shows that the nickel base alloy melt volume and its participation in the formation of the melt pool is notably higher than duplex stainless steel. One possible explanation for this phenomenon may be the reduced melting point along with an increased volume of the melt. Additionally, the greater absorption of the laser beam by the melted material could contribute to a larger melt volume when compared to the duplex side.

4.3. *Weld bead appearance*

The examination of the weld bead surface characteristics indicates that both the geometry of the weld bead and its surface roughness were notably influenced by variations in beam power and welding linear velocity.

An escalation in laser power from 300 W to 400 W, led to significant changes in the weld bead width and its surface concavity. (refer to Fig. 8a to c).

Specifically, through laser power augmentation up to the 400 W, the weld bead surface transitioned from a concave to a convex shape. At the lower power setting of 300 W, the input of laser beam energy was

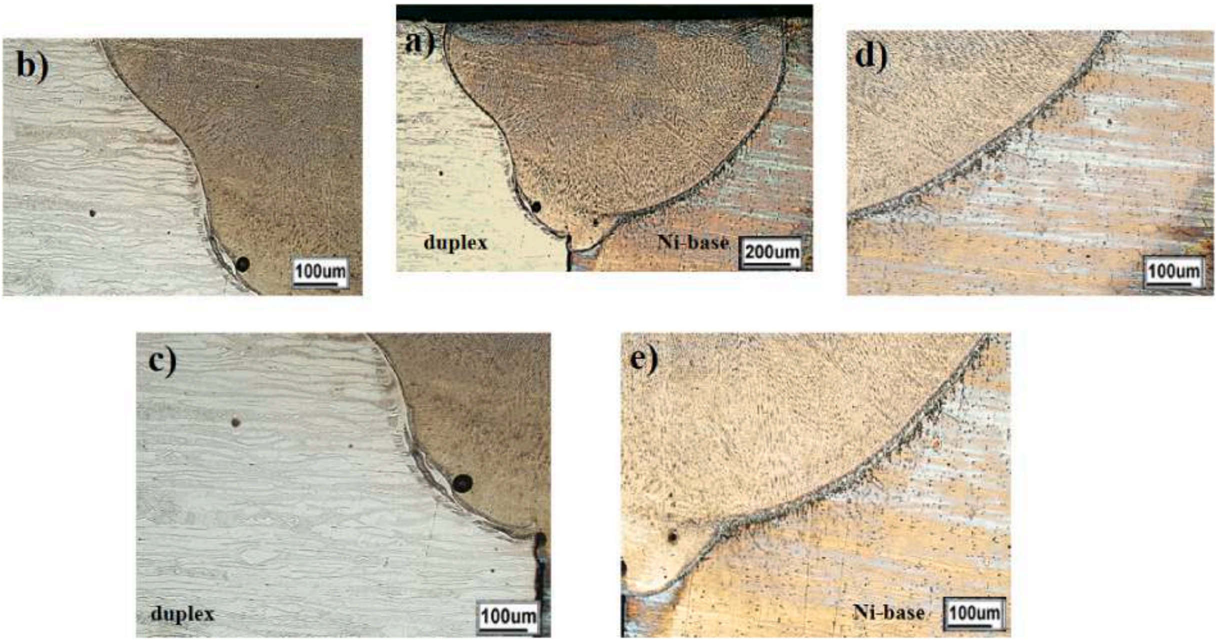

Fig. 10. Weld joint geometry at cross-section a) melt pool shape, b) fusion line at the duplex side, c) duplex base metal HAZ, d) Ni-base fusion line, e) Ni-base HAZ.

reduced, leading to a solidification rate that was considerably greater than the rates of heating and melting of the material.

Consequently, the melted material solidified almost instantly. In contrast, when the laser power was increased, some of the laser beam energy dissipated into the bulk material of the workpiece. Due to the small volume of the Ni-base material, heat accumulated, which caused the weld bead material to solidify at a slower rate. This resulted in a wider weld bead with greater overlap.

Fig. 8d–e demonstrate the reduction of beam linear velocity impact on the mechanism of weld bead formation. A decrease of speed from 300 to 200 mm/min results in a twofold increase in the weld bead width.

4.4. *Melt pool depth analysis*

The simultaneous influence of beam power and linear speed of welding on the maximum penetration depth is illustrated in Fig. 9. It was vividly shown that an evident beam power increment to 400 W created a complete molten pool depth of 1.5 mm. In contrast, variations in welding speed had a minimal impact on the molten pool depth when compared to the laser power augmentation. Consequently, laser power factor emerges as a notable factor in achieving the desired penetration depth. When the power level exceeded 400 W, the molten pool depth reached beyond 1.5 mm.

4.5. *Microstructural analysis*

Fig. 10 illustrates the melt pool geometry and mechanism at the laser power of 350 W. by passing the laser beam from the joint centre, the melting volume and its extension toward the Ni-base alloy were higher than the duplex side. Fig. 10b shows that the fusion line curve slope of the duplex side changed twice and the width of the fusion zone abruptly decreased at the middle depth of the fusion zone while at the Ni-base side, the slope of the fusion line changed gradually with the uniform curve slop (see Fig. 10d). At the lower part of penetration. (Fig. 10c–11e), The heat affected area and the keyhole region are observed. Interestingly, the porosity was formed at this region on both sides of the base metals with the bigger one at the duplex side. One possible reason could be different temperature gradients, limited area of the fusion zone and variation of the material flow due to the formation of the keyhole mechanism.

Fig. 11 depicts the microstructure near the line of fusion zone and base metals. Fig. 11a shows the duplex 2205 base metal which is formed from the austenitic grains distribution at the main ferrite matrix. At the HAZ of the duplex toward the fusion line, a narrow width mainly composed of delta ferrite microstructure was formed because of inducing the temperature of more than 800 °C. As illustrated in Fig. 11b, the epitaxial grain growth is observed at the line region between fusion zone and base metal, which can effectively reduce the stress concentration at the interface and has the characterization of base metal solidification mechanism and crystal growth at the fusion line region. The similar microstructural changes are reported in Ref. [27] for creating the epitaxial grain growth in Nd:YAG laser welding of Waspaloy and this analysis was performed through metallography analysis. The ASTM B637 alloy microstructure was established from a nickel matrix (γ), predominantly consisting of austenite grains, with a limited presence of carbide grain along with several irregularly shaped particles dispersed throughout the base metal as reported in Ref. [28].

Fig. 11c–d depicts the microstructural alterations extending from the nickel-based alloy fusion line toward the central regions of dissimilar fusion zone. Fig. 11c depicts a distinct microstructural pattern characterized mainly by columnar, cellular, and interdimeric regions, as shown in Fig. 11c–d. Typically, the columnar dendrites grow at various angles, oriented perpendicularly to the boundary line of the melt pool area and directed towards the heat transfer pathway which has been reported in Refs. [27,29]. The microstructural variation within the fusion zone during the welding process is significantly influenced by the solidification rate and the composition of the alloy. In case the distance from the melt pool center clearly increased, a significant change from dendritic to cellular-shaped inside grain boundaries was observed. The microstructural changes according to the variation of temperature gradient and solidification rate at different regions of the fusion zone and adjacent areas of Waspaloy was investigated in Ref. [27]. In dissimilar laser weld fusion zone, a considerable microstructural change inside the fusion zone toward nickel base alloy has had similar changes and is in agreement with the results highlighted in the previously mentioned research although minor changes were observed near the duplex fusion line.

The results obtained from EDS analysis shown in Table 3 and Fig. 12, the percentage of Fe significantly reduced from 43.6 to 29 percent by moving from the duplex workpiece, primarily base metal to the dissimilar mixed alloy melt pool. On the other hand, the nickel weight

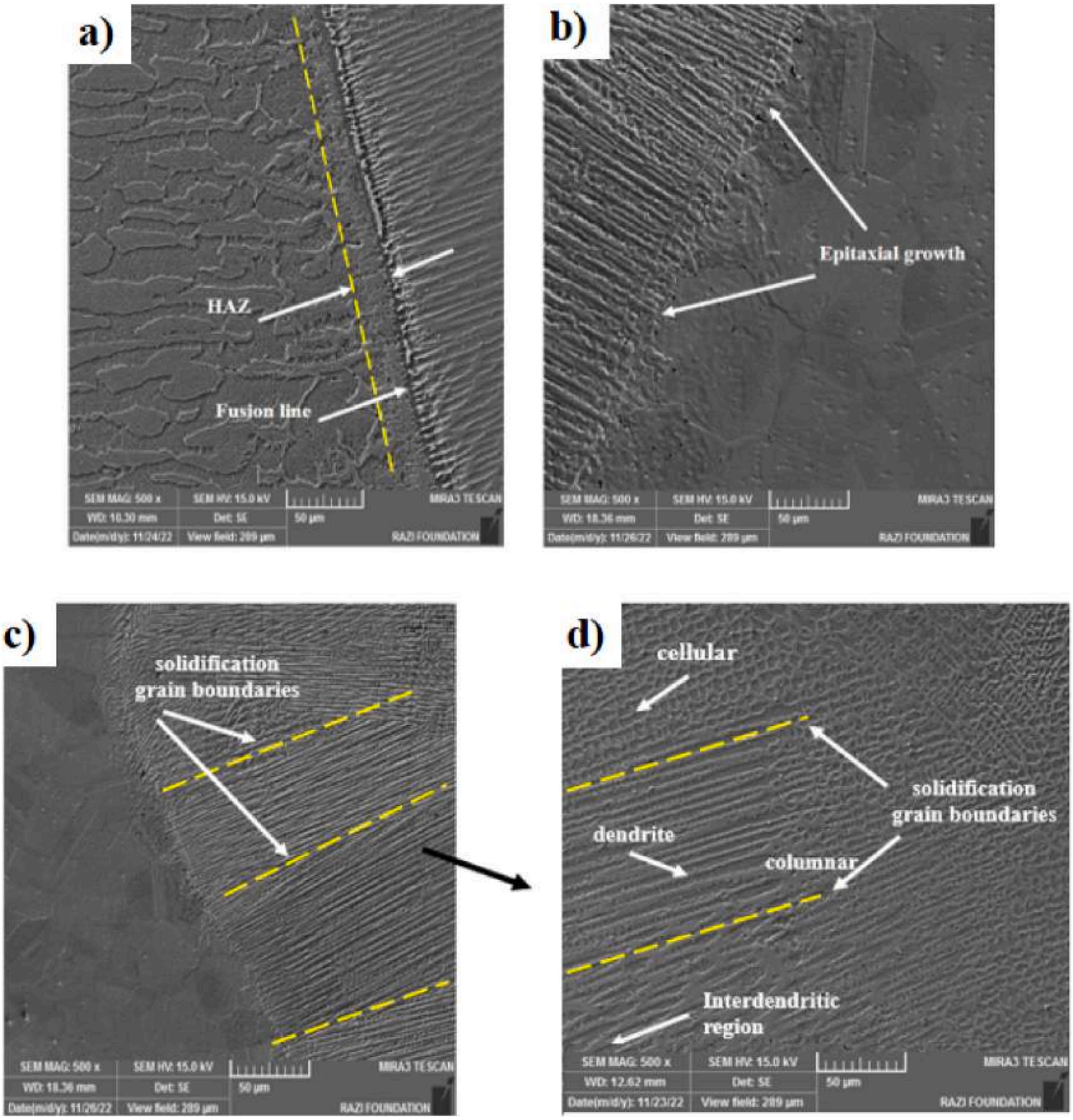

Fig. 11. SEM image from the microstructure of weld HAZ and base metals for a) duplex 2205 base metal, b) Ni-base alloy HAZ and base metal, c) near the boundary of fusion region for Ni-base alloy, d) at the fusion zone centre.

Table 3
EDS analysis for base metal of duplex 2205 and adjacent melted area.

Weld Area	Weld zone	Duplex	Ni-base
Element	Weight/(%)		
Al	0.4	0.05	**1.14**
Si	0.13	0.39	**0.07**
Ti	1.77	–	**2.66**
Cr	19.59	18.95	**19.02**
Mn	–	0.8	-
Fe	26.09	43.63	**0.68**
Co	6.51	6.53	**12.78**
Ni	28.96	6.86	**57.11**
Mo	16.26	29.32	**6.55**
C	–	–	
Total	**100**	**100**	**100**

percent reduced from 57 to 28 percent from nickel base metal to the fusion zone. Therefore, mixing alloys of two distinct sheets occurred at the weld fusion zone region because of such elemental composition. The Cobalt element was reduced from Ni-base alloy by about 50 percent, while Mo was reduced by about the same value percentage for Co from duplex sheet to the dissimilar melt pool. The weight percentage of elements of ASTM B637 alloy implied that it was rich in Ti, which could represent MC-type carbide grains as reported in Ref. [28]. The elements weight percentage variation analysis from the base metal to the center of fusion zone for duplex and Inconel 600 joint configuration has depicted combination of both base metals at the fusion zone with this discrepancy that the melt volume and participation of waspaloy alloy has been much greater than Inconel 600 which was reported in Ref. [2].

4.6. *Mechanical properties of the dissimilar joint*

The welded dissimilar joints' mechanical properties are directly influenced via weld geometry and its microstructure. These characteristics are determined by factors such as power of the beam, beam movement speed, position of the focal point and beam deflection. In this research, tensile stress-strain curves for both base metals and welded joints were analysed under varying laser powers and welding speeds to assess the performance of laser-welded joints across different parameters. To minimize the impact of errors on the results, tensile tests were conducted three times for each testing condition.

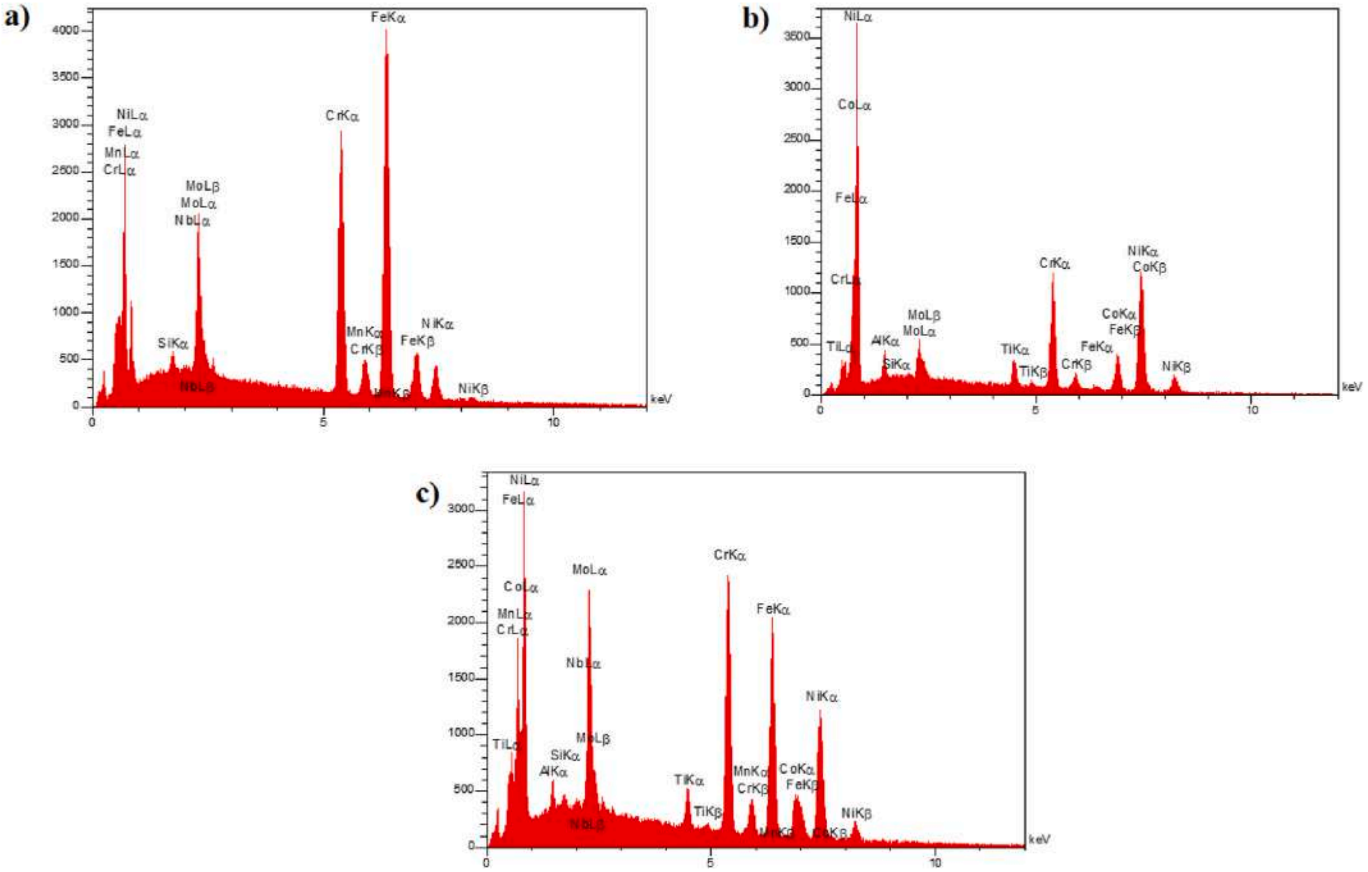

Fig. 12. EDS analysis pattern for a) duplex base metal, b) Ni-base alloy base metal, c) weld fusion zone.

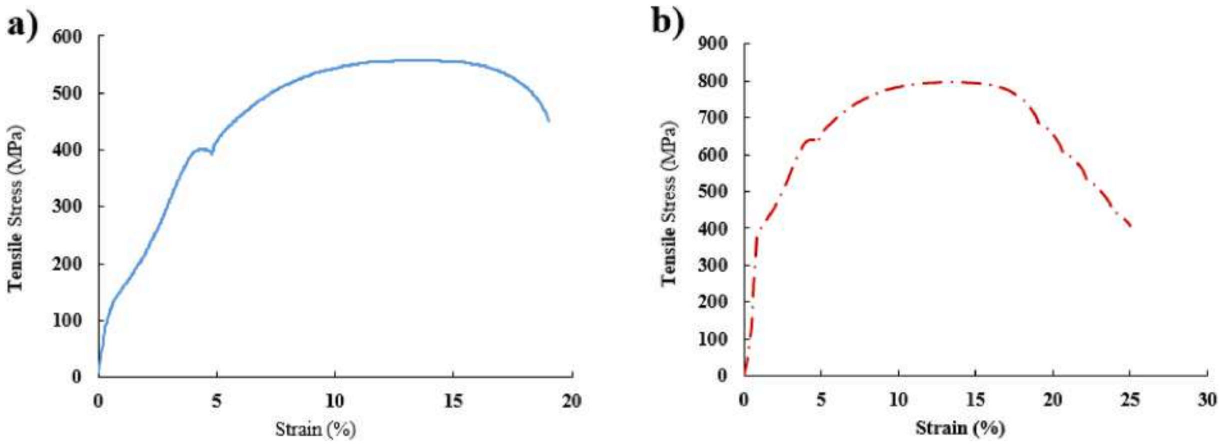

Fig. 13. The tensile stress/strain graph for base metals a) duplex stainless steel, b) Ni-base alloy.

Fig. 13a and b illustrate the graph of the tensile stress-strain rate of the base metals for duplex 2205 and Ni-base alloy orderly. It is clearly seen that the Ni-base alloy has had higher tensile stress about 200 MPa and a strain rate of about 8 percent. Therefore, it is anticipated the dissimilar welded samples failed from a region inside the fusion zone, HAZ of the duplex side or duplex base metal. Additionally, higher plastic deformation or elongation existed at the duplex side and tensile stress and strain properties may have a similar trend to the duplex steel side.

Fig. 14a illustrates the laser power influence on tensile stress/strain diagram of dissimilar joints. The laser power increased from 250 to 450 W, resulting in a significant rise in the elongation rate, which escalated from 3 percent to 19 percent. Concurrently, the tensile stress experienced an increase from 330 MPa to 570 MPa. Notably, a marked change in plastic deformation and elongation rate was observed by the laser power increment from 250 to 350 W. Further increasing the laser power from 350 to 450 W led to greater penetration depth and achieved the highest elongation rate.

It can be concluded that welding with higher energy density results in a larger melt volume and increases the tensile stress and strain rates, similar to those of the duplex base metal. However, at a laser power of 250 W, the melted pool did not penetrate sufficiently, causing the welded samples to fail at lower elongation and plastic deformation.

Fig. 14b illustrates the relationship between tensile stress and strain as influenced by variations in welding speed. It is evident that increasing

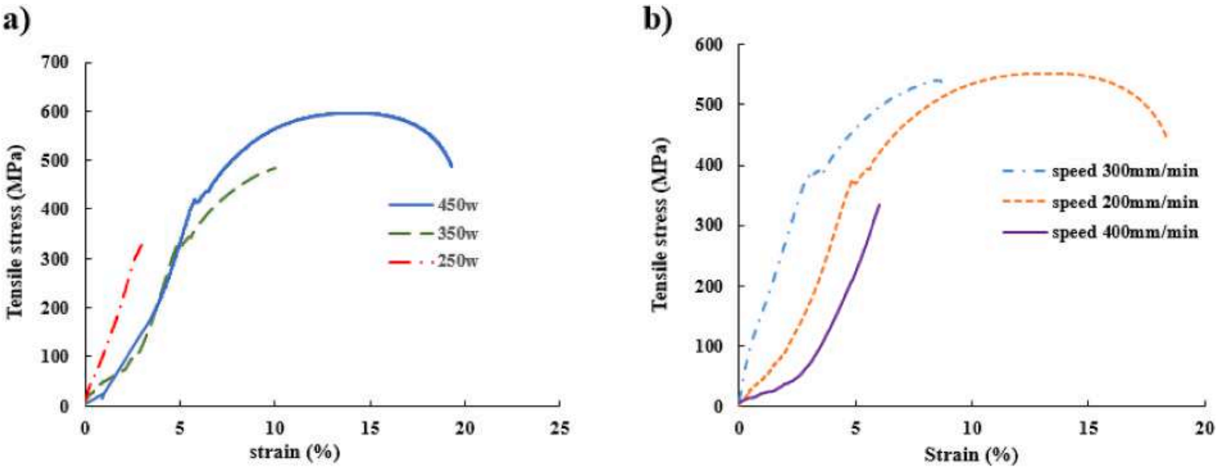

Fig. 14. The joint stress and strain rate according to the variation of a) laser power, b) welding speed.

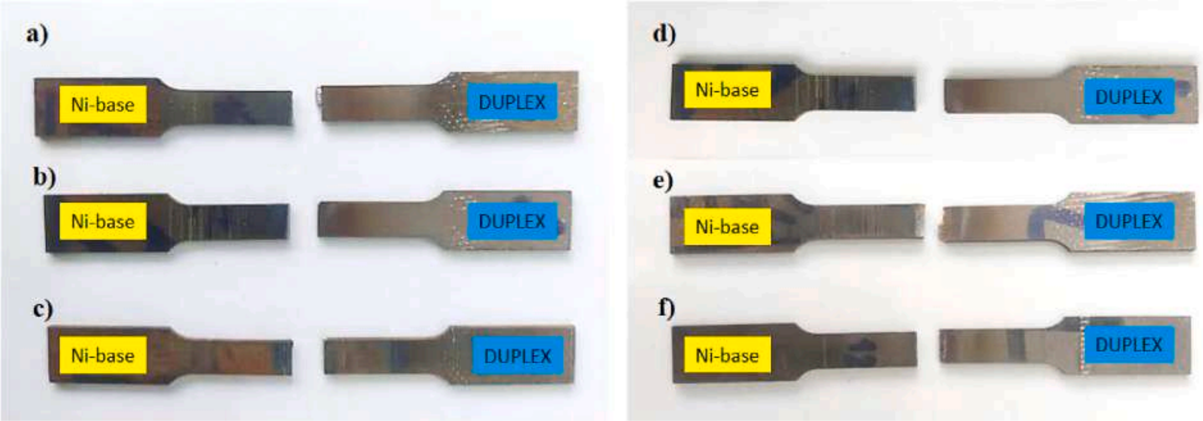

Fig. 15. Tensile samples appearance after failure at welding speed of 200 mm/min and laser power of a) 250 W, b) 350 W, c) 450 W and at laser power of 350w and welding speed of d)200 mm/min, e) 300 mm/min, f) 400 mm/min.

the velocity of welding speed from 200 to 400 mm/min, leads to a significant decrease in the elongation rate, which drops from 18 percent to 7 percent. This reduction can be attributed to a decrease in both the melt pool penetration depth and volume, resulting in lower values for both elongation rate and tensile stress. At linear speed of 200 mm/min, the maximum tensile stress recorded was approximately 520 MPa, accompanied by an elongation rate of 18 percent. The elongation rate decreased about 10 percent, when the linear speed was increased from 200 to 300 mm/min. Variation of welding speed from 300 to 400 W has had more influence on the weld bead width rather than penetration depth and microstructural changes. Furthermore, the increased cooling rate associated with a higher welding speed of 300 mm/min results in a significantly greater tensile stress in relation to the relative strain compared to the welding speed of 200 mm/min. This variation is attributed to the formation of distinct portions of dendritic microstructure and the resulting temperature gradient. In another study, it was reported that due to the formation of the large Laves phases, there is a possibility of fracture during plastic deformation, leading to a significant reduction in the elongation rate of the welded joint made from Inconel 718 and duplex 2205 [21]. Therefore, it could be said that apart from weld bead geometry, the microstructure composed of dendritic microstructure had a reduction impact on the weld joint strain which is not the aim of this study.

Fig. 15 depicts the samples of the tensile test under varying conditions of movement speed and laser beam power. Fig. 15a–c illustrate the appearance of failed samples by increment of the laser power up to 400 W. Specifically, Fig. 15a presents the failed surface at the lower laser power of 300 W, originating from the weld region. The incomplete weld penetration and the inferior mechanical properties of the fusion zone resulted in failure of all welded samples from this zone. However, by increasing the laser power, the ultimate tensile stress of the weld joint became comparable to that of the duplex 2205 base metal. Fig. 15d–f demonstrate the influence of welding speed on the fracture appearance of welded joints during tensile testing. As the linear speed of welding was reduced to 200 mm/min, the fracture location shifted from the duplex melted line to the Ni-base alloy side. The beam movement speed reduction increases the melt pool volume, necessitating greater energy and elongation to separate the dissimilar joint.

Fig. 16 illustrates the of laser power impact on the fracture surface of the tensile test samples on both sides toward each base metal. Fig. 16a–c shows the laser power augmentation impact on the fracture surface toward the duplex side. The depth of cavities notably increased by laser power augmentation up to 450 W. Also, a ductile fracture mechanism with more dimples is observed in Fig. 16b–c. Fig. 16d–f shows the laser power effect on the ASTM B637 alloy side. By increasing the laser power, a ductile fracture mechanism is observed along with bigger core and cavities which demonstrate that the samples have had more plastic deformation toward the ASTM B637 side.

Fig. 17 illustrates the influence of beam linear speed on the both sides of the weld joint fracture surface. Fig. 17a–c demonstrate how an increase in welding speed affects the fracture surface of the samples. As depicted in Fig. 17a, the fracture surface exhibits a ductile fracture

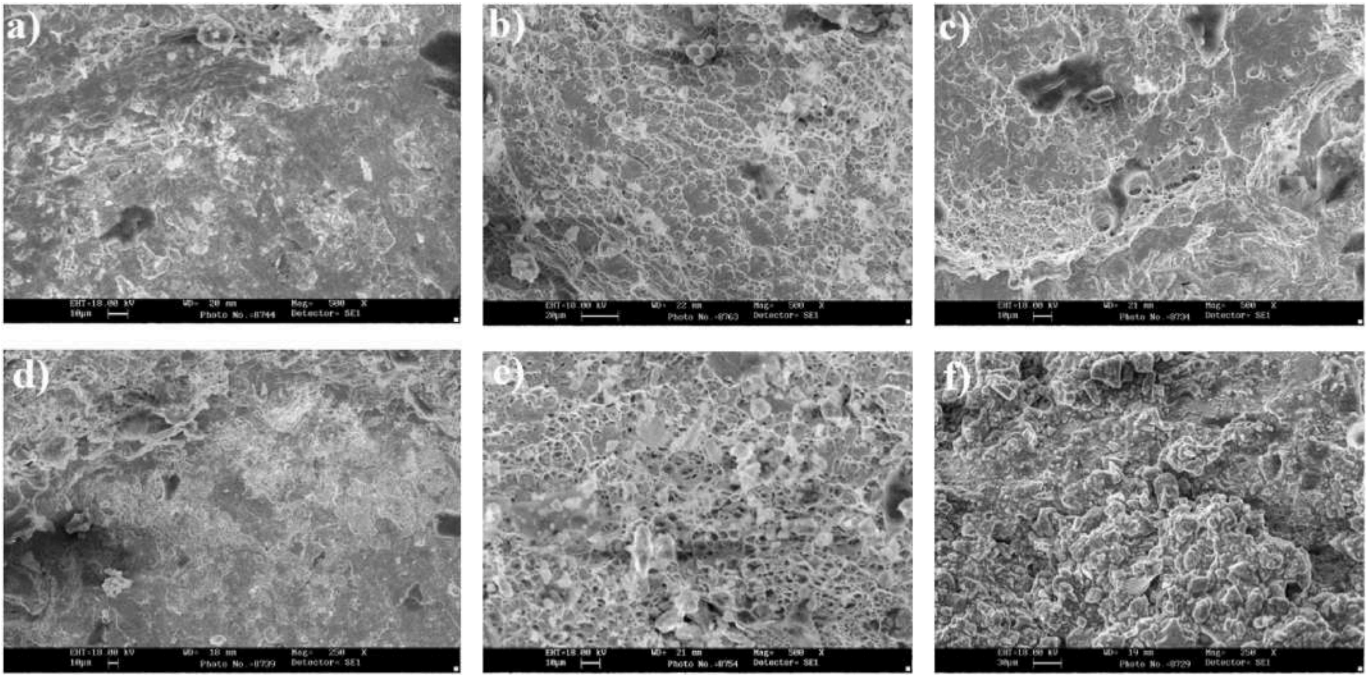

Fig. 16. Dissimilar joint fracture surface of tensile tests samples for the duplex side at the welding speed of 20 0 mm/min and different laser power of a) 300 W, b) 350 W, c)400 W, fracture surface for Ni-base side at laser power of d) 300 W, e) 350 W, f) 400 W.

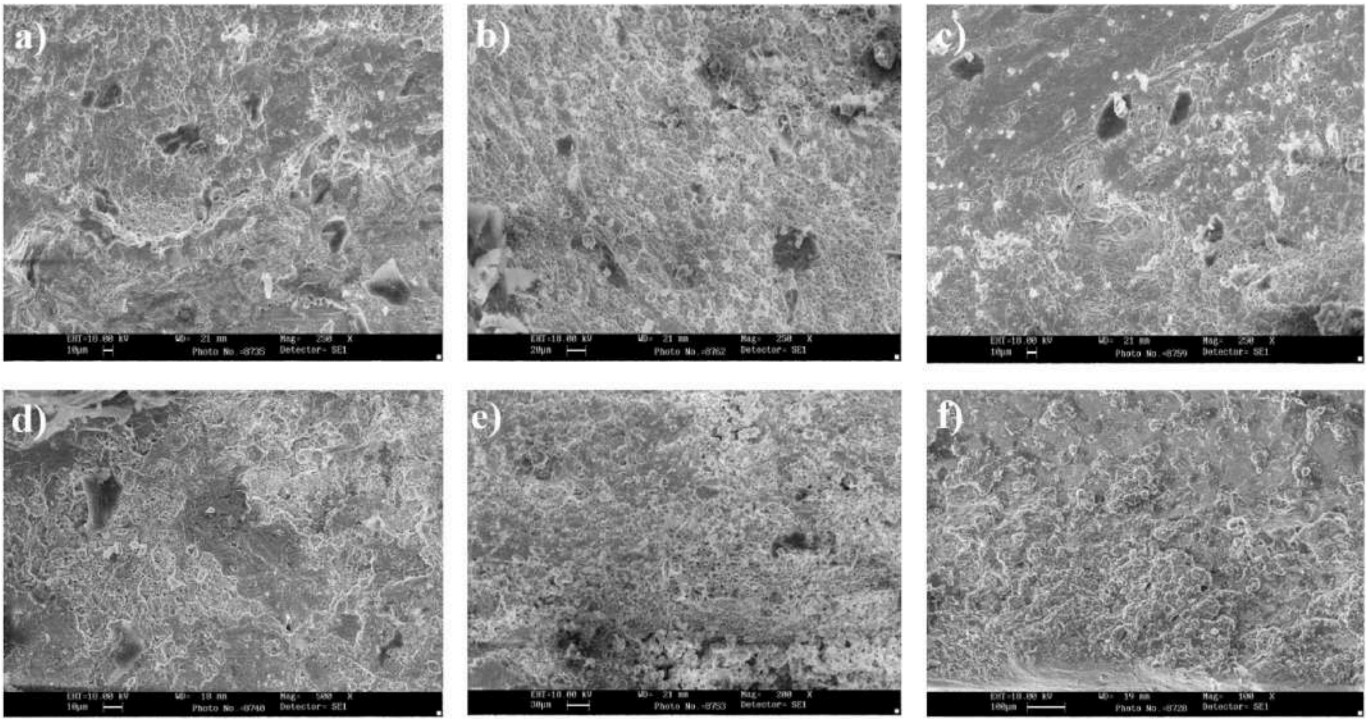

Fig. 17. Dissimilar joint fracture surface of tensile tests samples for the duplex side at a laser power of 400w and different welding speed of a) 200 mm/min, b) 300 mm/min, c) 400 mm/min, fracture surface for Ni-base side at a different welding speed of d) 200 mm/min, e) 300 mm/min, f) 400 mm/min.

characterized by larger cavities at low linear speed. As observed in Fig. 17c, at a speed of 400 mm/min, both the depth and quantity of cavities are significantly reduced, indicating a predominance of brittle fracture mechanisms on the fracture surface. Fig. 17d–f further illustrate the impact of welding speed on the fracture surface of the nickel-based alloy. At a lower welding speed of 200 mm/min, as shown in Fig. 17d, a greater depth of cavities is noted, accompanied by a higher number of dimples, indicating a ductile fracture mode. By the welding speed increases, the number of dimples and the depth of cavities noticeably decrease, suggesting a transition in the fracture mode from ductile to brittle, as evidenced in Fig. 17e–f.

5. Conclusion

This study examined the effects of key fiber laser welding parameters on the temperature distribution, molten pool formation, and mechanical properties of dissimilar joints between duplex stainless steel (DSS) 2205 and ASTM B637. The results demonstrated that laser power, beam deflection, and welding velocity played a crucial role in influencing the thermal field and fusion characteristics. The temperature on the duplex stainless steel side exhibited a 30 % increase when laser power was raised from 300 W to 400 W, highlighting the asymmetry in heat absorption between the two alloys.

Furthermore, tensile strength was significantly affected by laser power, beam velocity, indicating their direct impact on the mechanical integrity of the welded joint. Numerical simulations confirmed that the high-temperature region (above 1400 °C) expanded considerably with increasing laser power, with duplex stainless steel experiencing a more pronounced temperature rise than ASTM B637. Microstructural analysis revealed a transition in growth modes near the fusion line, where columnar dendrites formed at the interface, gradually shifting to dendritic and cellular structures toward the weld center. Elemental composition analysis showed that Fe content decreased from 43.6 % to 29 % from the duplex base metal to the fusion zone, while Ni content reduced from 57 % to 28 % on the nickel-based side. These variations confirm the occurrence of elemental mixing in the molten pool, significantly influencing the resulting microstructure and mechanical properties.

Regarding mechanical performance, an increase in welding speed from 200 mm/min to 400 mm/min led to a notable decrease in elongation rate from 18 % to 7 %, whereas raising the laser power from 250 W to 450 W resulted in an elongation increase from 3 % to 19 %. Additionally, higher laser power promoted the formation of a ductile fracture mechanism, characterized by larger dimples and cavities, particularly on the ASTM B637 side, demonstrating greater plastic deformation in the nickel-based alloy region. Overall, the findings of this study provide valuable insights into creating dissimilar geometry and materials properties in fibre laser welding to improve weld quality, structural integrity, and mechanical performance. These results can contribute to enhancing industrial welding processes where DSS 2205 and ASTM B637 are utilized in demanding applications.

CRediT authorship contribution statement

Amir Parsian: Writing – original draft, Validation, Software, Methodology, Data curation. **Mohammad Akbari:** Writing – original draft, Validation, Supervision, Software, Methodology. **Arash Karimipour:** Writing – original draft, Validation, Software, Methodology, Conceptualization. **Mahdi Rafiei:** Writing – original draft, Formal analysis, Data curation, Conceptualization. **Mohammad Mehdi Razzaghi:** Writing – original draft, Resources, Investigation.

Consent to participate

Not applicable.

Availability of data and material

The raw/processed data required to reproduce these findings cannot be shared at this time due to technical or time limitations.

Code availability

Not applicable.

Ethics approval

Not applicable.

Consent for publication

Not applicable.

Declaration of competing interest

The authors declare that they have no known competing financial interests or personal relationships that could have appeared to influence the work reported in this paper.

Data availability

Data will be made available on request.

References

[1] A.K. Maurya, C. Pandey, R. Chhibber, Dissimilar welding of duplex stainless steel with Ni alloys: a review, Int. J. Pres. Ves. Pip. 192 (2021) 104439, https://doi.org/10.1016/j.ijpvp.2021.104439, 2021/08/01/.

[2] A. Soleimani, M. Akbari, A. Karimipour, A.H. Meghdadi Isfahani, R. Nosouhi, Investigation the effect of dissimilar laser welding parameters on temperature field, mechanical properties and fusion zone microstructure of inconel 600 and duplex 2205 stainless steel via response surface methodology, Heliyon 10 (4) (2024) e26010, https://doi.org/10.1016/j.heliyon.2024.e26010.

[3] G.N. Ahmad, M.S. Raza, N. Singh, H. Kumar, Experimental investigation on ytterbium fiber laser butt welding of inconel 625 and duplex stainless steel 2205 thin sheets, Opt Laser. Technol. 126 (2020) 106117.

[4] K.D. Ramkumar, et al., Metallurgical and mechanical characterization of electron beam welded super-duplex stainless steel UNS 32750, J. Manuf. Process. 16 (4) (2014) 527–534.

[5] S. Saravanan, K. Raghukandan, N. Sivagurumanikandan, Pulsed nd: YAG laser welding and subsequent post-weld heat treatment on super duplex stainless steel, J. Manuf. Process. 25 (2017) 284–289.

[6] P. Luchtenberg, P.T. de Campos, P. Soares, C.A.H. Laurindo, O. Maranho, R. D. Torres, Effect of welding energy on the corrosion and tribological properties of duplex stainless steel weld overlay deposited by GMAW/CMT process, Surf. Coating. Technol. 375 (2019) 688–693.

[7] G.N. Ahmad, M.S. Raza, N.K. Singh, G. Muvvala, Investigating the effect of process parameters on weld pool thermal history and mechanical properties of laser welded inconel 625 and duplex stainless steel 2205 dissimilar welds, Optik 248 (2021) 168134, https://doi.org/10.1016/j.ijleo.2021.168134, 2021/12/01/.

[8] M. Tumer, T. Karahan, T. Mert, Evaluation of microstructural and mechanical properties of dissimilar inconel 625 nickel alloy–UNS S32205 duplex stainless steel weldment using MIG welding, Weld. World 64 (1) (2020) 21–35, https://doi.org/10.1007/s40194-019-00825-x, 2020/01/01.

[9] G. Padmanabham, B. Shanmugarajan, Laser-based joining of metallic and non-metallic materials, Laser-Assisted Fabricat.Mater. (2013) 159–220.

[10] P. Jovičević-Klug, M. Rohwerder, Sustainable new technology for the improvement of metallic materials for future energy applications, Coatings 13 (11) (2023) 1822.

[11] A. Karimi, A. Karimipour, M. Akbari, M.M. Razzaghi, M.J. Ghahderijani, Investigating the mechanical properties and fusion zone microstructure of dissimilar Laser weld joint of duplex 2205 stainless steel and A516 carbon steel, Opt Laser. Technol. 158 (2023) 108875.

[12] A.E. Odermatt, V. Ventzke, F. Dorn, R. Dinsé, P. Merhof, N. Kashaev, Effect of laser beam welding on microstructure, tensile strength and fatigue behaviour of duplex stainless steel 2205, J. Manuf. Process. 72 (2021) 148–158, https://doi.org/10.1016/j.jmapro.2021.10.020, 2021/12/01/.

[13] A. Baghdadchi, V.A. Hosseini, K. Hurtig, L. Karlsson, Promoting austenite formation in laser welding of duplex stainless Steel—Impact of shielding gas and laser reheating, Weld. World 65 (2021) 499–511.

[14] I. Calliari, C. Gennari, E. Hurtado Delgado, A. Miranda Perez, B. Rodriguez Vargas, Laser welding of plastically deformed lean duplex stainless steel, Metallurgia Italiana 1 (2018) 5–10.

[15] A. Ghosh, P. Kalvettukaran, D. Misra, and S. K. Acharyya, "Experimental Investigation on the Effect of Pulse Width on Laser Welding of 2205 Duplex Stainless Steel.".

[16] H. Gozarganji, A. Farnia, M. Ebrahimnia, Effect of shielding gas composition on geometry and austenite formation in low power pulsed nd: YAG laser welded 2205 duplex stainless steel, Arch. Metall. Mater. 66 (2021).

[17] G.N. Ahmad, M.S. Raza, N. Singh, G. Muvvala, Investigating the effect of process parameters on weld pool thermal history and mechanical properties of laser welded inconel 625 and duplex stainless steel 2205 dissimilar welds, Optik 248 (2021) 168134.

[18] M. Azari, E. Rasti, M.H.R. Dehkordi, H. Azimy, A. Zarei, S.A. Bagherzadeh, Investigation of temperature distribution and melt pool microstructure in laser fusion welding of inconel 625 superalloy, J. Laser Appl. 33 (2) (2021) 022015.

[19] S.K. Sharma, K. Biswas, A. Nath, I. Manna, J.D. Majumdar, Microstructural change during laser welding of inconel 718, Optik 218 (2020) 165029.

[20] S. Madhankumar, S. Ashwin, J. Ajai Robert, J. Clifford Francis, R. Bavan Kalyan, A. Krithik Raj, W. Joel Anton, Experimental investigation on ultimate tensile

strength of laser butt welded inconel 718 alloy and 2205 duplex stainless steel, Mater. Today : proceedings 45 (2021) 6783–6787.

[21] Yiming Shen, Lishan Wang, Li Liangliang, Dehai Kong, Ruyu Ma, Liping Liu, Li Pengfei, Microstructure evolution of 2205 duplex stainless steel (DSS) and inconel 718 dissimilar welded joints and impact on corrosion and mechanical behaviour, Mater. Sci. Eng., A 929 (May 2025) 148136.

[22] Aritra Ghosh, Dipten Misra, Kumar Sanjib, Experimental and numerical investigation on laser welding of 2205 duplex stainless steel, Lasers in Manufacturing and Materials Processing 6 (2019) 228–246.

[23] Niraj Kumar, Chandan Pandey, Prakash Kumar, Dissimilar welding of inconel alloys with austenitic stainless-steel: a review, J. Pressure Vessel Technol. 145 (2023). ASME.

[24] S. Saravanan, N. Sivagurumanikandan, K. Raghukandan, Effect of heat input on microstructure and mechanical properties of nd: YAG laser welded super duplex stainless steel-numerical and experimental approach, Optik 185 (2019) 447–455.

[25] Tlili Iskander, Baleanu Dumitru, Sajadi S. Mohammad, Ghaemi Moram Ferial A. Fagiry, Numerical and experimental analysis of temperature distribution and melt flow in fiber laser welding of inconel 625, Int. J. Adv. Des. Manuf. Technol. 121 (2022) 765–784.

[26] Nawaz Ahmad Gulshad, Mohammad Shahid Raza, N.K. Singh, Hemant Kumar, Experimental investigation on ytterbium fiber laser butt welding of inconel 625 and duplex stainless steel 2205 thin sheets, Opt Laser. Technol. 126 (2020).

[27] Shoja Razavi Reza, Laser beam welding of waspaloy: characterization and corrosion behavior evaluation, Opt Laser. Technol. 82 (2016) 113–120.

[28] M.D.M. das Neves, A. Lotto, J.R. Berretta, W.d. Rossi, N.D.V. Júnior, Microstructure development in nd: YAG laser welding of AISI 304 and inconel 600, Weld. Int. 24 (10) (2010) 739–748.

[29] Li Zhang, S.L. Gobbi, F. Bonollo, A. Tiziani, G. Fontana, Metallurgical investigation of laser welds in wrought waspaloy, Sci. Technol. Weld. Join. 3 (1998).